frontiers | Frontiers in Marine Science

TYPE Original Research
PUBLISHED 24 February 2023
DOI 10.3389/fmars.2023.1141926

OPEN ACCESS

EDITED BY
Wei Li,
South China Sea Institute of Oceanology (CAS), China

REVIEWED BY
Jingbo Nan,
Southern University of Science and Technology, China
Yazhou Fu,
Institute of Geochemistry (CAS), China

*CORRESPONDENCE
Yao Guan
guanyao@mail2.sysu.edu.cn
Xiaoming Sun
eessxm@mail.sysu.edu.cn

†These authors have contributed equally to this work

SPECIALTY SECTION
This article was submitted to Marine Biogeochemistry, a section of the journal Frontiers in Marine Science

RECEIVED 11 January 2023
ACCEPTED 10 February 2023
PUBLISHED 24 February 2023

CITATION
Ren Y, Guan Y, Sun X, Xu L, Xiao Z, Deng Y and He W (2023) Nano-mineralogy and growth environment of Fe-Mn polymetallic crusts and nodules from the South China Sea. *Front. Mar. Sci.* 10:1141926. doi: 10.3389/fmars.2023.1141926

Nano-mineralogy and growth environment of Fe-Mn polymetallic crusts and nodules from the South China Sea

Yingzhi Ren[1,2†], Yao Guan[3,4*†], Xiaoming Sun[1*], Li Xu[1], Zhenglian Xiao[5], Yuqi Deng[4] and Wentao He[4]

[1]School of Marine Sciences, Guangdong Provincial Key Laboratory of Marine Resources and Coastal Engineering, Sun Yat-sen University, Guangzhou, China, [2]Key Laboratory of Marine Mineral Resources, Guangzhou Marine Geological Survey, Guangzhou, China, [3]Key Laboratory of Tropical Marine Ecosystem and Bioresource, Fourth Institute of Oceanography, Ministry of Natural Resources, Beihai, China, [4]Guangxi Key Laboratory of Beibu Gulf Marine Resources, Environment and Sustainable Development, Fourth Institute of Oceanography, Ministry of Natural Resources, Beihai, China, [5]Southern Marine Science and Engineering Guangdong Laboratory (Zhuhai), Zhuhai, China

Fe-Mn polymetallic crusts and nodules from the South China Sea (SCS) consist of submarine ferromanganese (Fe-Mn) oxide precipitates, and represent important marine mineral resource with substantial economic and scientific research value. Previous studies on the SCS polymetallic crusts and nodules were mainly focused on their bulk mineralogy and geochemistry, whilst research on their nanomineralogy is still lacking. In this study, transmission electron microscopy (TEM), Raman spectroscopic mapping, and in-situ micro X-ray diffraction (XRD) analysis were conducted on the nano-mineralogy of the SCS polymetallic crusts and nodules. It is found that the SCS polymetallic crusts and nodules consist mainly of layered/columnar/mottled nano-phase Fe-Mn minerals and detritus such as quartz, feldspar, and clays. Also, an independent Ti mineral phase has been documented, and the mineralogical analysis reveals the transformation from vernadite to birnessite and todorokite. Titanium forms colloidal minerals in seawater and precipitates into the crusts and nodules with other colloids, such as FeOOH and Si-Al. Vernadite and birnessite can be transformed to todorokite with stable structure under sub-oxic conditions. Therefore, the SCS polymetallic crusts and nodules were formed in a short period of sub-oxic environment and diagenetic process, and the transformation can influence the enrichment of Ni and other metals during the crust/nodule growth.

KEYWORDS

nano-mineralogy, high resolution transmission electron microscope (HRTEM) analysis, growth environment, polymetallic crusts and nodules, South China Sea

1 Introduction

Marine Fe-Mn ferromanganese (Fe-Mn) oxide precipitates are mainly formed by direct precipitation from the ambient cold seawater (hydrogenetic-type), sediment pore water (diagenetic-type), or seafloor hydrothermal fluids (hydrothermal-type) (Hein et al., 1997; Hein et al., 2013; Bau et al., 2014). According to the deposition environments, marine Fe-Mn precipitates are classified into crusts, nodules, and hydrothermal Fe-Mn deposits. Fe-Mn (or Co-rich) polymetallic crusts are commonly deposited on substrates without sediment cover, e.g., on the outer margin of seamount summits and marine platforms or saddle structures (Halbach et al., 2017; Usui et al., 2017), whilst Fe-Mn polymetallic nodules are deposited on intermountain basins or abyssal plains with more sediment cover, and tend to grow around a core. All the Fe-Mn polymetallic crusts, nodules, and hydrothermal deposits are important marine mineral resource and host critical metals such as Co, Ni, Cu, Tl, Te, Nb, and rare earth elements plus yttrium (REY) (Hein et al., 2013), and have received much research and exploration interest.

In recent years, the Fe-Mn polymetallic crusts and nodules in marginal seas have received increasing attention, esp. those in the Baltic Sea (Grigoriev et al., 2013; Yli-Hemminki et al., 2016) and the California continental margin (Hein, 2005; Conrad et al., 2017). Several mineralogical and geochemical studies on the Fe-Mn crusts and nodules in the South China Sea (SCS) have also been carried out (Li and Zhang, 1990; Bao and Li, 1993; Lin et al., 2003; Zhang and Weng, 2005; Zhang et al., 2009; Wang and Zhang, 2011; Zhang et al., 2013; Zhong et al., 2017; Guan et al., 2017a; Guan et al., 2017b; Guan et al., 2017c; Guan et al., 2019; Jiang et al., 2019; Zhou et al., 2021; Konstantinova et al., 2022).

Polymetallic crusts and nodules are widely distributed on the SCS seafloor (Li and Zhang, 1990; Zhong et al., 2017), including in the northern continental slope (around the Dongsha (Pratas) Islands), the northwestern continental margin (around the Zhongjian (Trition) Island), the central sea basin [around the Huangyan Island (Scarborough Shoal)], and around the Nansha Islands (Spratly islands). The SCS polymetallic crusts and nodules were developed mainly on the terraces and seamounts of continental slope at 472 to 3570 m water depth. The Fe-Mn encrustation is generally thin (few mm to cm). Previously, the SCS polymetallic crusts and nodules are generally considered to have a hydrogenetic origin (Zhang et al., 2013; Guan et al., 2017b), but later studies also suggested major involvement from gas hydrate release (Zhong et al., 2017) and biogenesis (Jiang et al., 2019). Microzonal analysis revealed that the northern SCS nodules may have had a mixed hydrogenetic-diagenetic genesis (Guan et al., 2019; Zhong et al., 2019).

Analyzing the growth structure and mineralogy of polymetallic crusts and nodules is essential for studying this kind of marine mineralization, and techniques such as XRD, *in-situ* XRD, synchrotron XRD, and transmission electron microscopy (TEM) are widely used, as minerals from polymetallic crusts and nodules are generally poorly crystalline (Bai et al., 2002; Kashiwabara et al., 2013; Manceau et al., 2014; Marcus et al., 2015; Atkins et al., 2016; Lee et al., 2016; Lee and Xu, 2016a, b; Shiraishi et al., 2016; Konstantinova et al., 2017). Mineralogical studies on the SCS polymetallic crusts and nodules were focused mainly on whole-rock mineral phase characterization, whereas in-depth studies on *in-situ* mineralogical characterization and nano-minerals are still inadequate (Zhong et al., 2017; Guan et al., 2017b).

Previous studies have shown that micro-structures in the SCS polymetallic crusts and nodules are mainly growth structures and intermittent structures. Common growth structures include mottled, stacked, laminated, columnar and palisade structures. These structures are composed mainly of Fe-vernadite, todorokite (10 Å manganite), birnessite, amorphous Fe-oxides/hydroxides, quartz, and feldspars (Guan et al., 2017b; Guan et al., 2019). Zhong et al. (2017) found that the northwestern SCS nodules contain large amount of pyrite, asbolite and apatite. The SCS polymetallic crusts and nodules are mainly composed of poorly-crystallized Fe-Mn hydroxides, and manganese oxides. The poor crystallization often leads to complex mineral identification, esp. for some Fe-phase minerals (often amorphous), which cannot be determined with XRD. Therefore, the TEM analyses would allow accurate identification of multiple mineral phases in these polymetallic crusts and nodules.

As mentioned above, the SCS polymetallic crusts and nodules contain kinds of minerals and metallic minerals have poor crytallinity, which makes them ideal samples for nano-mineralogy research. Furthermore, the nano Fe-Mn minerals have strong surface chemical activity and selective adsorption capacity, which is of great significance to the selective enrichment of ore-forming elements in the polymetallic crusts and nodules (Guan et al., 2017b). And the study of nano-minerals is beneficial in revealing the mechanism of element enrichment and mineralization of the polymetallic crusts and nodules.

2 Geological setting

The SCS lies at the intersection of the Eurasian, Indo-Australian, and Philippine Sea plates. It is a marginal sea located south of South China, with an area of ~3.50×10^4 km^2 (Figure 1). Regional surveys suggested that the SCS slopes in a stepwise manner from the margin to the center with increasing water depth (200-3800 m), with the development of undulatory topography comprising continental shelf and slope, island shelf and slope, and marginal sea basin (Yang et al., 2015). Isobath of the northern continental shelf is relatively straight, and the width decreases from west to east. Meanwhile, water depth of the northern continental shelf increases gradually from northwest to southeast, whilst the gradient first increases and then decreases. Gradient of the western continental shelf is narrow and steep; the water depth of the western continental shelf varies greatly, the topography is undulating and complex, with the development of sea platforms, terraces, ridges, and troughs. The eastern island slope is located west of the Philippine Islands, with a maximum water depth of 4,000 m and an average gradient of 1.4°. The topography is obviously undulating, with geographical entities such as ridges, troughs, slopes, and deep-water terraces. The SCS basin is located in the central, developing deep-sea plains, seamount chains, and seamount groups,

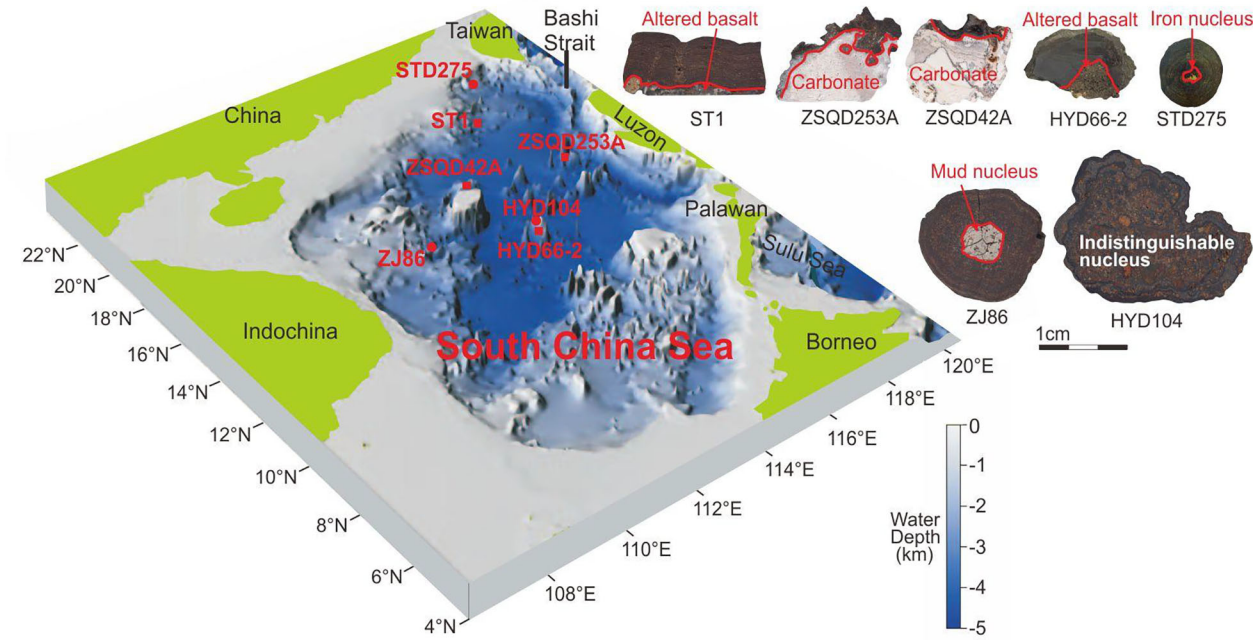

FIGURE 1
Location and topographic map of the South China Sea (Wang and Li, 2009).

etc. The water depth is between 4000-4500 m. The topography is generally flat, but the elevation difference of seamounts is large (> 3000 m). Therefore, the tectonic and geological background of the SCS and the good water exchange capacity are both favorable for the growth and mineralization of the polymetallic crusts and nodules.

3 Samples and analytical methods

3.1 Samples

Our samples of the SCS crusts and nodules were collected by seafloor trawling on the Guangzhou Marine Geological Survey research vessel "Haiyangsihao" during the 2011-2012 SCS survey. Detailed information of the samples is given in Guan et al. (2017b). Polymetallic crust samples (ST1, ZSQD251A, ZSQD253A, ZSQD42A, and HYD66-2) have platy or crustal Fe-Mn encrustations and hard substrate of altered basalt and carbonates (e.g., reef limestone). Most samples have friable thin (0.1-1.9 cm) Fe-Mn encrustations and are (dark) brown or black. Polymetallic nodule samples (STD275, ZJ86, and HYD104) are spherical, ellipsoidal, elongate, conodont, or irregular. They have Fe-Mn encrustations around the cores (iron oxides, clayey, muddy, or altered basalt). The nodules grow on top or surrounded by coarse sandy to clayey sediments (Table 1).

3.2 Petrographic analysis

The samples are cut along the growth profile to make polished thick sections (thickness ~100 μm), and then observed with a ZEISS Imager and an A2m optical microscope (reflected light). Photographs were processed with the Axio Vision 4.8 software.

3.3 Laser Raman spectroscopy

The analysis was conducted at the School of Marine Science, Sun Yat-sen University (SYSU), using a ThermoFisher DXR2xi laser Raman micro-spectrometer equipped with a 532 nm argon ion laser and edge filters. Both spot analysis and mapping were performed. The map was formed by multiple line analyses. The analysis conditions include 3 mW laser energy, 6 μm beam size, 0.2 s exposure time, 10 scans, 600 × 600 μm sweep range, and 8 μm mapping resolution. Data processing utilized the ThermoFisher's OMSNICxi and OMSNIC software.

3.4 XRD analysis

The analysis were conducted at the School of Marine Science, SYSU, using a Rigaku D/max Rapid II micro-area X-ray diffractometer (Japan). In the XRD analysis of bulk samples, the crusts and nodules were washed with ultrapure water and dried in a blower for 24 h (drying temperature set at 30°C), then ground to 200-mesh using an agate mortar. In the *in-situ* micro XRD analysis, particle samples with a diameter of <3 mm were observed with an optical microscope equipped on the X-ray diffractometer, and then adjust the selected microarea to the center of the field of view.

The instrument parameters include Mo target and 0.1 mm collimator, 50 kV voltage, 30 mA current, and XRD data acquisition on a 2-D image plate detector. All samples were

TABLE 1 Sample descriptions and bulk mineralogy of Fe-Mn crusts and nodules from the South China Sea.

Sample	Type	Locations	Water depth (m)	Substrate/Nucleus	Major minerals
ST1	crust	117.9104°E 20.4674°N	1600	Altered basalt	δ-MnO2, quartz and anorthite
ZSQD253A	crust	118.6061°E 16.7664°N	1150	Carbonate	δ-MnO2, quartz, anorthite and calcite
ZSQD42A	crust	114.8172°E 16.8493°N	1230	Carbonate	δ-MnO2, quartz, anorthite and calcite
HYD66-2	crust	115.2729°E 13.6789°N	1378	Altered basalt	δ-MnO2, todorokite, quartz and anorthite
STD275	nodule	118.2791°E 21.6915°N	1548	Iron nucleus	δ-MnO2, quartz and anorthite (with goethite and feroxyhyte in the nucleus)
ZJ86	nodule	112.5245°E 15.3421°N	1945	Mud nucleus	δ-MnO2, todorokite, quartz and anorthite
HYD104	nodule	116.1818°E 15.5635°N	815	Undiscernible or no nucleus	δ-MnO2, todorokite, birnessite, quartz and clinochlore

analyzed twice under the same conditions, and the signals were combined to improve the signal-to-noise ratio. The 2-D data were then converted to 1-D spectra using Rigaku's 2DP software. Identification of the major minerals was done with the PDXL2 software.

3.5 TEM analysis

The high-resolution TEM (HRTEM) imaging and selected-area electron diffraction (SAED) analyses were completed at the Analysis Center of SYSU on a JEOL JEM-2010 transmission electron microscope (Japan), and at the Guangzhou Institute of Geochemistry, Chinese Academy of Sciences, on a FEI Talos F200S transmission electron microscope (USA).

(1) JEM-2010: The powder sample (200-mesh) was dispersed in alcohol and dropped onto a Cu grid (with a carbon film microgrid), using a disposable dropper and then allowed to dry naturally. The TEM operating voltage is 200 kV, and the instrument is equipped with an INCA energy spectrum. The analysis site was selected first under microscope at low magnification, and observed with energy-dispersive X-ray spectroscopy (EDS) at higher magnification, followed by high resolution phase analysis at ultra-high magnification.

(2) Talos F200S: The samples were made by secondary embedding-ultra-thin sectioning. Each sample was dispersed in ultrapure water by ultrasound, which was then dropped onto the pre-consolidated resin, dried with a blower, and re-embedded in resin afterward. The resin was heated with a blower, solidified, and cut with a Leica ultrathin microtome (USA), and then placed on a Cu mesh (with carbon-coated film) and dried. The instrument operates at 200 kV with maximum 1.5M× magnification and ≤ 0.25 nm resolution. The instrument is equipped with an EDAX energy spectrum with ≤ 136 eV energy resolution. Fast Fourier transform (FFT) and other TEM image processing were performed with the TIA TEM Imaging and Analysis software (version 4.15).

4 Results

4.1 Microscopic structure characteristics

The encrustations of the SCS polymetallic crusts and nodules contain light and dark Fe-Mn mineral layers, with medium-coarse crystalline silicates and bioclasts being cemented or encapsulated by Fe-Mn minerals (Figures 2, 3). Microstructural features of the samples are very similar, with primary growth structures being lamellar, columnar, or mottled, and secondary ones being concentric or dendritic.

By comparing the Raman spectra (Mn-O peak signal) maps and microscopic photographs, we find that the Mn-O peak intensity correlates positively to the density of growth structure (Figure 4). The Mn-O peak intensity is similar to the light and dark changes of the growth layer, which indicates that the changes in the growth structure and the growth layer of the crust (core) are the alternating changes in the mineral composition.

4.2 Mineral compositions

Previous studies have shown that Fe-Mn crusts and nodules consists mainly of Mn (Fe-vernadite and todorokite) and Fe (goethite, lepidocrocite, amorphous ferrihydrite) phase minerals, together with minor clay minerals, calcite, apatite and detrital quartz and feldspars (Rajani et al., 2005; Pattan and Parthiban,

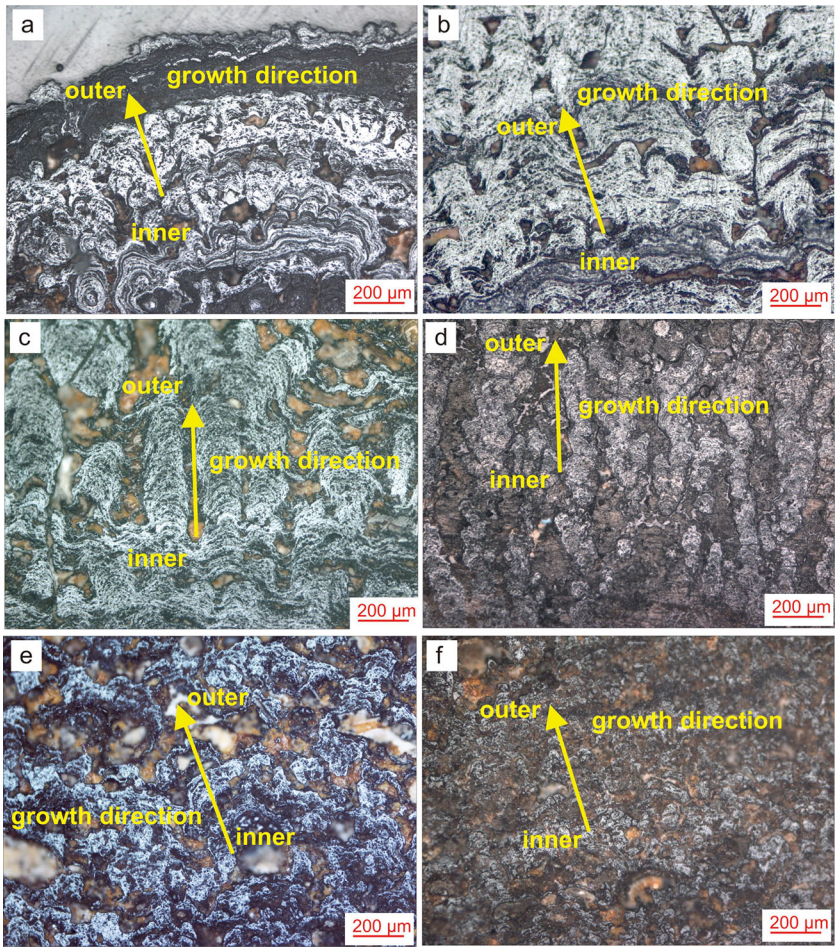

FIGURE 2
Photos of main growth structure of the SCS polymetallic crusts and nodules **(A, B)** laminated structure, **(C, D)** columnar, structure, **(E, F)** taxitic structure).

2007; Xu, 2013; Zhou, 2016; Zhong et al., 2017). Characteristic XRD peaks of different Mn minerals in our samples include (Figure 5): 0.239 and 0.140 nm (vernadite), 0.72, 0.35 and 0.24 nm (birnessite), and 0.97, 0.48, 0.24 and 0.14 nm (todorokite and buserite). The characteristic diffraction peaks of todorokite are at 9.56 Å (100) and 4.78 Å (covering (200) and (002)). Meanwhile, the 4.26 Å $(100)_{quartz}$, 3.34 Å $(011)_{quartz}$, 2.45 Å $(110)_{quartz}$, and 1.37 Å $(203)_{quartz}$ diffraction peaks represent the better-crystallized quartz, whilst the 3.84 Å $(104)_{calcite}$, 3.02 Å $(113)_{calcite}$, 2.08 Å $(202)_{calcite}$, 1.90 Å $(018)_{calcite}$, and 1.86 Å $(116)_{calcite}$ diffraction peaks represent Mg-calcite, which is mainly derived from biological detritus (mainly foraminifera). Most samples have an undulating background peak with peaks centered at ca. 2.4 and 1.4 Å. This background represents the presence of amorphous ferrihydrite (Lee et al., 2016). Our results show that the SCS polymetallic crusts and nodules comprise mainly Fe-vernadite (δ-MnO_2), quartz, feldspars, and amorphous ferrihydrite. This is consistent with the findings by Guan et al. (2017b), although some minerals (e.g., apatite) reported by that study were not found here.

Under the microscope, the SCS polymetallic crusts and nodules display black Fe-Mn encrustations with grape-like or massive structure. *In situ* micro-XRD analysis results indicate that the Fe-Mn crusts are mainly composed of Fe-vernadite and todorokite, with many light-colored minerals (mainly quartz and feldspars) interspersed among the Fe-Mn minerals (Figure 6).

4.3 Nano-mineralogy

In the TEM dark field, there are numerous nano-particles in the samples (Figure 7). Based on the XRD results, we further analyze the SAED patterns and the TEM-EDS data, and the major minerals in the samples are recognized. In particular, the form and composition of birnessite and todorokite are very similar, so it will be confirmed by SAED pattern after each EDS analysis (Figures 7, 8). In samples ST1 and ZSQD253A (Figures 7A–C), there are numerous nano-particles of quartz, thin clay mineral layers, network of Fe-vernadite (δ-MnO_2), and amorphous flocs of FeOOH. Sample ZJ86 contains birnessite and todorokite as well (Figures 7F–H). The EDS results show that the birnessite is mainly associated with Na, K, Ca, and Ni, while todorokite is mainly associated with Ca and Ni.

We found that independent Ti minerals are common in the SCS crusts and nodules (Figure 8). In the TEM dark field, Ti minerals exist

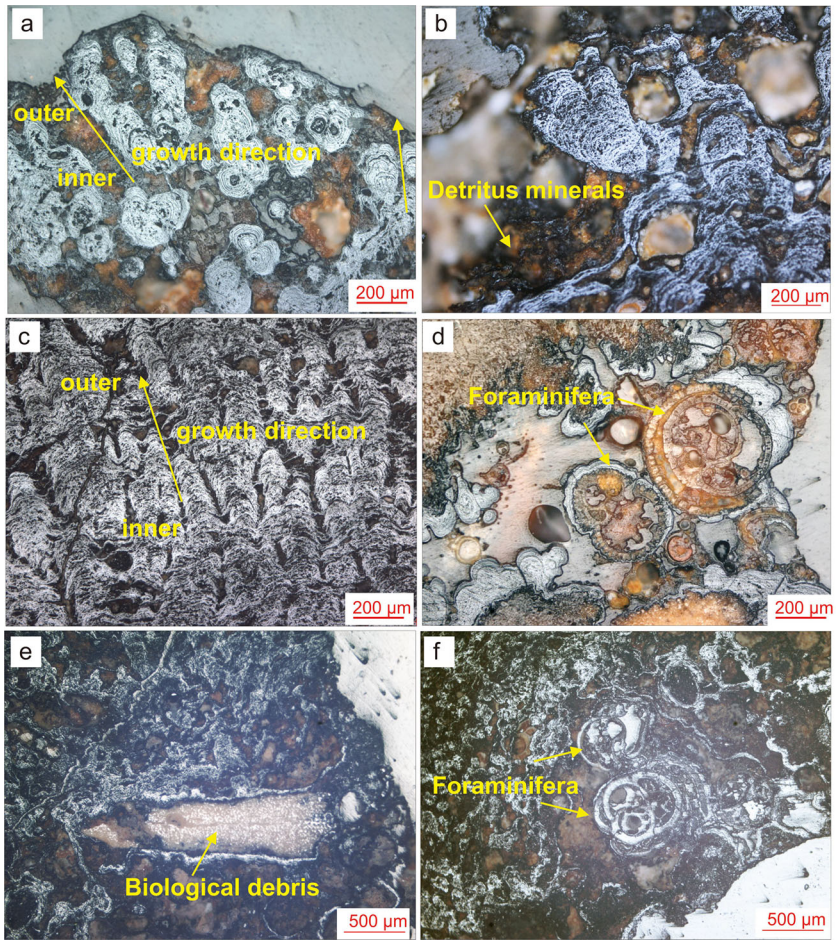

FIGURE 3
Photos of secondary growth structures of the SCS polymetallic crusts and nodules **(A)** concentric circle micro-nodules and columnar structure; **(B)** palmar-print structure; **(C)** dendritic structure; **(D–F)** biological debris and foraminifera in the encrustations).

in a flocculent form, which is very similar to the colloidal morphology of amorphous FeOOH and Si-Al hydrate. Meanwhile, Ti minerals occur in the form of nanofragments in the high-resolution bright field. The EDS results show that the flocculent Ti minerals contain certain Fe and Si. Its high-resolution photograph and the FFT results show [_37_4] the crystallographic stripes in (_403), (111), and (51_2) under the crystallographic band axis, and the measured crystallographic spacing under the Z-axis is 3.58 Å. Therefore, the Ti minerals were determined as hydrated Ti oxide (e.g. $H_2Ti_3O_7$, Kataoka et al., 2013).

5 Discussion

5.1 Microstructure and hydrodynamic environment

In this study, the growth profiles of the SCS polymetallic crusts and nodules were found to contain different microstructure assemblages (Figure 9). Xu (2013) summarized that the growth structures of the crusts and nodules can be divided into primary and secondary ones, while different structure assemblages representing different growth rates and bottom currents. The alternating growth of different Fe-Mn layers implies fluctuations in the growing conditions, which may reflect periodic changes of seawater environment in the South China Sea.

Based on the growth structure characteristics, we suggest that the SCS polymetallic crusts and nodules may have formed in four growth stages (Figure 9). Columnar, palisade, and dendritic structures are predominant in the early growth stage. In this stage, the dendritic structure indicates the inconsistent growth rates at various locations on the same growth surface, while the formation of columnar structure indicates a low hydrodynamic growth environment and a higher formation growth rate (Xu, 2013). The second growth stage developed mainly lamellar (and some mottled) structures, which indicates that the bottom current and oxidation conditions are weak (Xu, 2013). The third growth stage mainly developed mottled structures, which reflects strong bottom current and turbulent seawater environment (Xu, 2013; Guan et al., 2017b). Laminar and mottled structures are mainly developed in the fourth growth stage, indicating that the bottom current and oxidation environment in this stage are more reduced than the previous stage (Guan et al., 2017b).

We also found that the SCS polymetallic crusts and nodules from near the continental margin contain mainly mottled structures. This indicates that they were grown in a more turbulent depositional

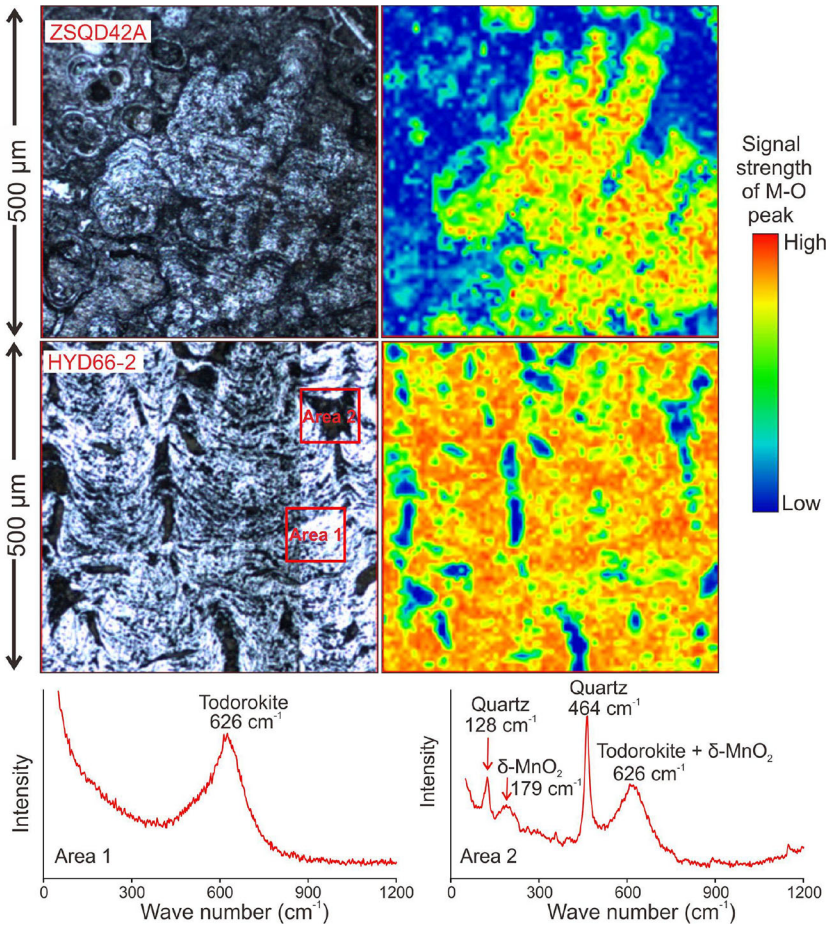

FIGURE 4
Raman mapping results of the selected area in the samples ZSQD42A and HYD66-2.

environment, and were strongly influenced by coastal currents and terrestrial debris (Zhong et al., 2017). In contrast, polymetallic crusts and nodules near the central basin (e.g., HYD66-2 and HYD104) mostly develop laminae and columnar structures. This indicates that they grew in a more stable bottom flow, and were less influenced by terrestrial input (Zhong et al., 2017).

5.2 Mineral composition and depositional environment

Mineralogical characteristics are important in determining the genetic type of Fe-Mn crusts and nodules (Bau et al., 2014) and the ore-metal enrichment mechanism. The XRD spectral peaks of Mn minerals are all broad, indicating poor crystallization, and the presence of todorokite suggests that the SCS polymetallic crusts and nodules may have grown in a short period of sub-oxic seawater environment (Conrad et al., 2017).

According to the intensity of XRD (Figure 5) and chemical composition (Guan et al., 2017b), samples from the northern SCS samples (e.g., ST1, STD275) have large amount of detrital quartz and feldspar. This suggests that these SCS crusts and nodules obtain many terrestrial materials. Samples ZSQD42A, and ZSQD253 from around the Zhongsha Island areas contain large amounts of calcite and biological debris (Table 1), suggesting input from marine organisms on the polymetallic crust/nodule mineralization. In contrast, samples near the central basin (e.g., HYD66-2 and HYD104) contain significant amounts of Mn minerals and less detrital minerals (quartz and feldspar, Figure 5), consistent with their columnar and dendritic growth structures that suggest a stable growth environment and insignificant terrestrial input. Todorokite in crust samples HYD66-2 (Figure 5) and ST1 (Figure 6) indicates the prevalence of todorokite in the SCS polymetallic crusts and nodules, yet its content is likely very low (undetected by XRD). Todorokite in crusts and nodules usually forms in suboxic condition (Conrad et al., 2017), the low content of todorokite in the SCS polymetallic crusts and nodules suggested that they have experienced suboxic environment. As mentioned above, the SCS crusts and nodules are of hydrogenetic origin. Therefore, we propose that the SCS crusts and nodules have been exposed a suboxic environment (Guan et al., 2019), but the process may have been of short duration or not suboxic enough to affect their overall hydrogenetic signatures. According to Figure 6, the SCS crusts contain a low content of todorokite expect for HYD66-2. The reason for more todorokite in HYD66-2 is that the location of this sample grows near the central basin and more possible to be exposed to a suboxic environment.

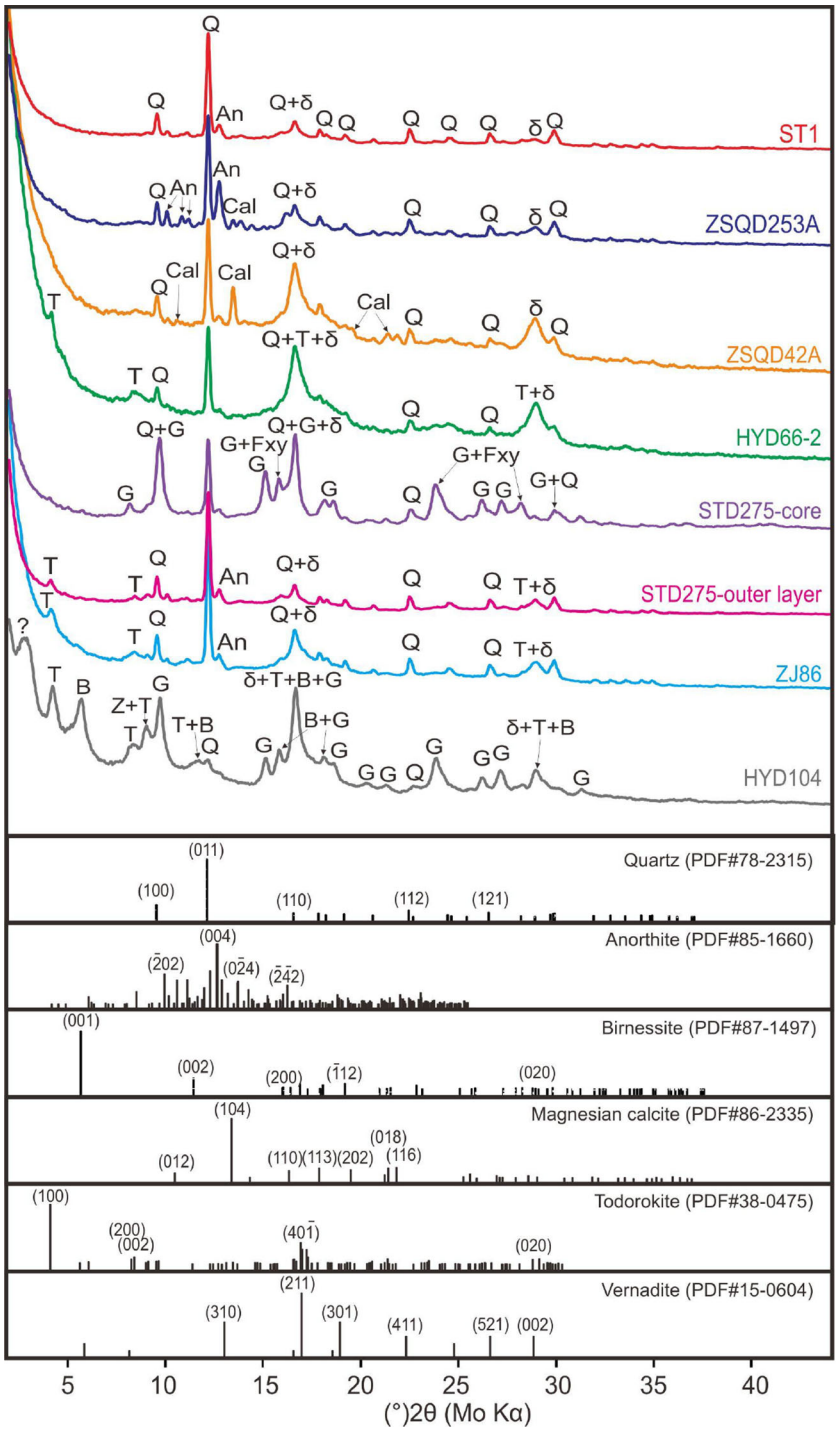

FIGURE 5
XRD patterns of the SCS polymetallic crusts and nodules (Q, quartz; An, Anorthite; Cal, calcite; T, todorokite; G, goethite; B, birnessite; Z, Chloro zeolite).

5.3 The existing phase of Si, Ti, Fe hydroxides

Silicon can precipitate directly into the polymetallic crusts and nodules as quartz and clay minerals, and occur in seawater in colloidal precipitates or as anion complexes (Akagi, 2013; Tréguer and de la Rocha, 2013). EDS spectra of Si is present in all the samples (Figure 7), which indicates good supply of Si during the crust/nodule growth and accompanied by the precipitation of Fe-Mn oxides into the crusts and nodules, and the layered clay minerals often coexist with the Mn minerals. This may be due to the similar layered structure of vernadite and birnessite (both clay minerals). In addition, the mineral interlayers of birnessite are negatively charged (Halbach et al., 2017) and can accommodate

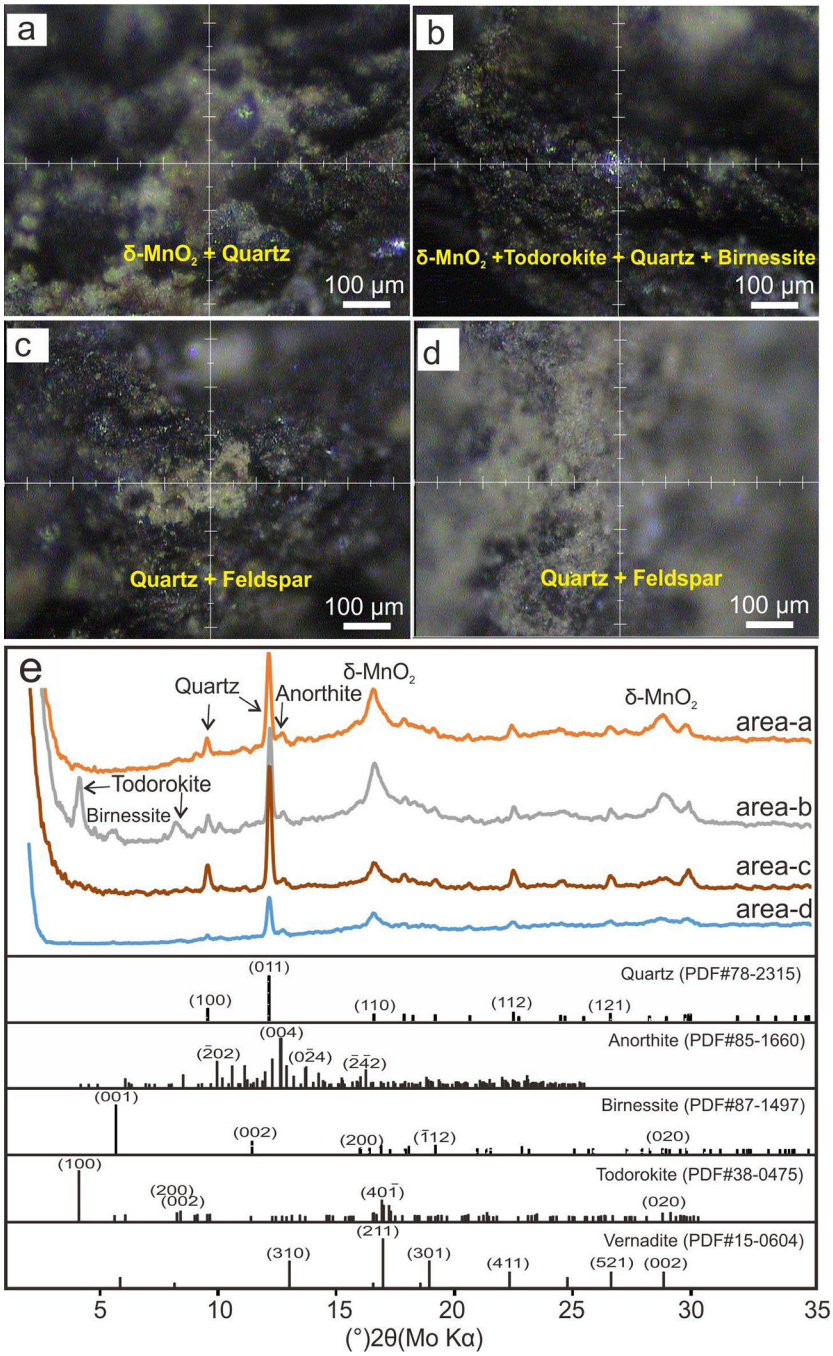

FIGURE 6
In-situ micro-XRD patterns of sample ST1. **(A, B)** Mn minerals including δ-MnO_2 and todorokite. **(C, D)** light-colored minerals including quartz and feldspar. **(E)** XRD patterns of area a-d.

cations (e.g., K^+, Ca^+) and even water molecules (Manceau et al., 2014; Lee and Xu, 2016b). This shows strong adsorption properties similar to those of clay minerals. In addition to the layered minerals, many flocculent minerals can be seen in the TEM dark-field phase, which are mostly colloidal minerals of Si, Al and FeOOH.

The hydrated oxide of Ti ($H_2Ti_3O_7$) was first reported by Izawa et al. (1985), and its crystal structure determined by Kataoka et al. (2013). $H_2Ti_3O_7$ is a hydrate of TiO_2, and occurs mainly in colloidal form in aqueous solution. In this study, we first observed Ti minerals in the SCS polymetallic crusts and nodules, and the EDS result shows that these Ti minerals mainly contained Ti and O. However, the SAED pattern could not match any Ti-O minerals data. Nevertheless, the evidences in this study were not enough to support the proposal of a newfound Ti mineral. Because the nodules and crusts grow in the seabed environment, and previous studies have already suggested that Ti entered the nodules in a colloidal chemical way (Koschinsky and Hein, 2003). We speculate that these independent Ti minerals might be a kind of Ti hydroxide, which

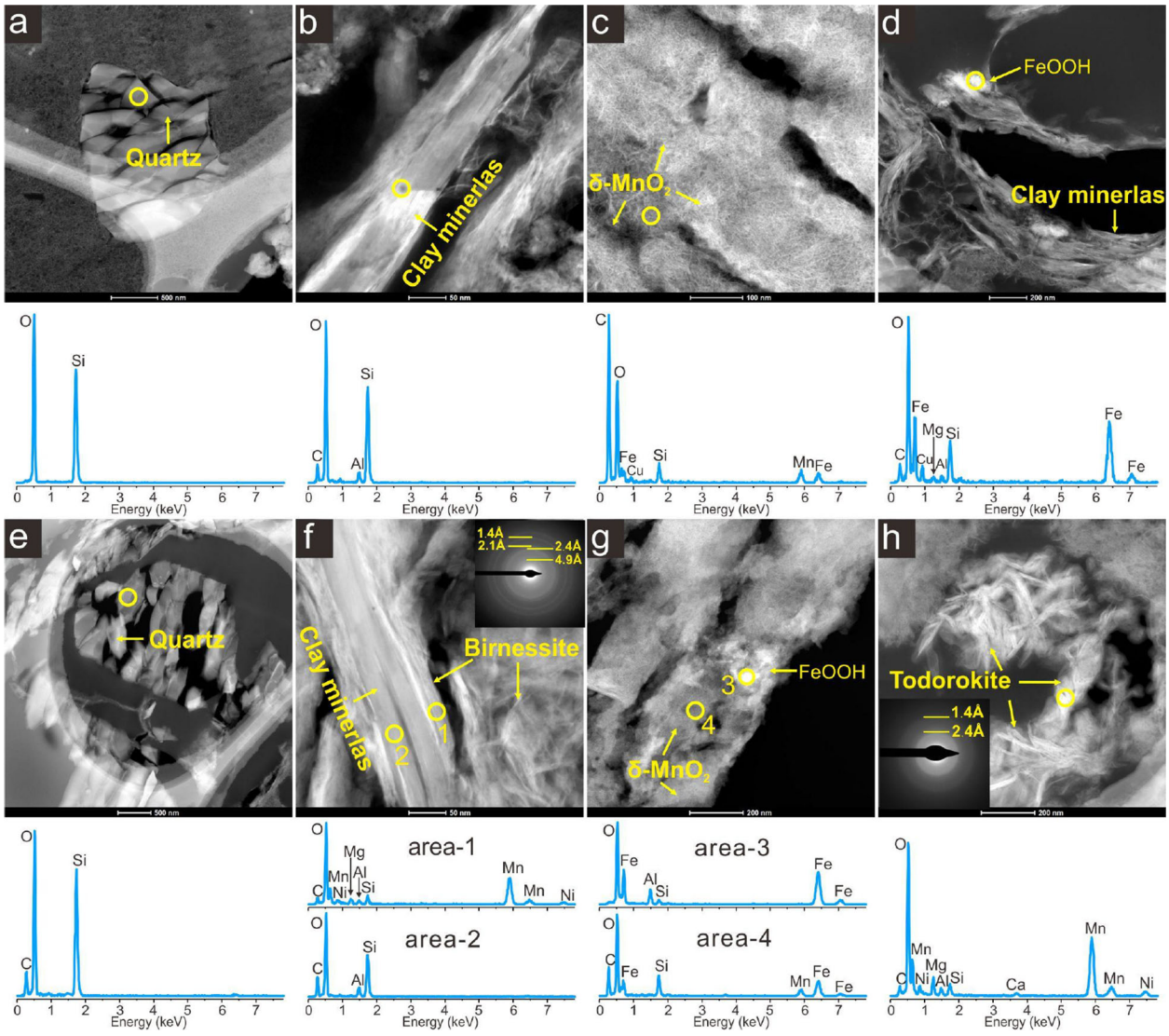

FIGURE 7
TEM photos and micro-*in-situ* EDS patterns of samples ST1 **(A–C)**, ZSQD253A **(D, E)**, and ZJ86 **(F–H)** in the TEM dark field.

was temporarily indicated by $TiO_2{\cdot}xH_2O$ in this study. These Ti minerals perhaps indicated that Ti could form colloidal minerals in seawater and enter directly into the crusts and nodules.

The surface of hydrated FeOOH and Ti oxides is positively charged in seawater, which facilitates selective adsorption of some seawater anions or anion complexes (Koschinsky and Hein, 2003; Jiang et al., 2011). In addition, colloids can aggregate (through covalent bonds) and eventually co-precipitate (Bruland et al., 2014). In this study, we inferred that these colloidal hydrated Ti and Fe oxides were concentrated into the polymetallic crusts and nodules (together with colloidal aggregates, incl. $SiO_2{\cdot}xH_2O$ or $Al_2O_3{\cdot}xH_2O$ in seawater), as evidenced by the widespread presence of colloidal flocs of Fe, Ti, Si, and Al in the samples (Koschinsky and Halbach, 1995). Fluvial and aeolian input can carry substantial terrestrial substance (incl. Si and Al) to the South China Sea, which dissolves rapidly and forms colloids in the seawater, and then re-precipitates in Fe-Mn oxides/hydroxides. Therefore, terrestrial influence on mineral composition of the SCS polymetallic crusts and nodules includes not only the direct detrital input, but also the later re-precipitation of dissolved materials or colloids.

5.4 Mn-phase minerals and their intraconversion

Previous studies have shown that vernadite, birnessite, and todorokite are the three major Mn-phase minerals in marine Fe-Mn crusts and nodules (Usui et al., 1989; Bodeï et al., 2007). In general, vernadite (δ-MnO_2) is a good indicator mineral for hydrogenetic origin, while todorokite and 10 Å phyllomanganate often occur in diagenetic and hydrothermal origins respectively (Takahashi et al., 2007; Manceau et al., 2014; Pelleter et al., 2017). For example, some Fe-Mn growth layers at the bottom of oceanic polymetallic nodules (buried in sediments) were subjected to early

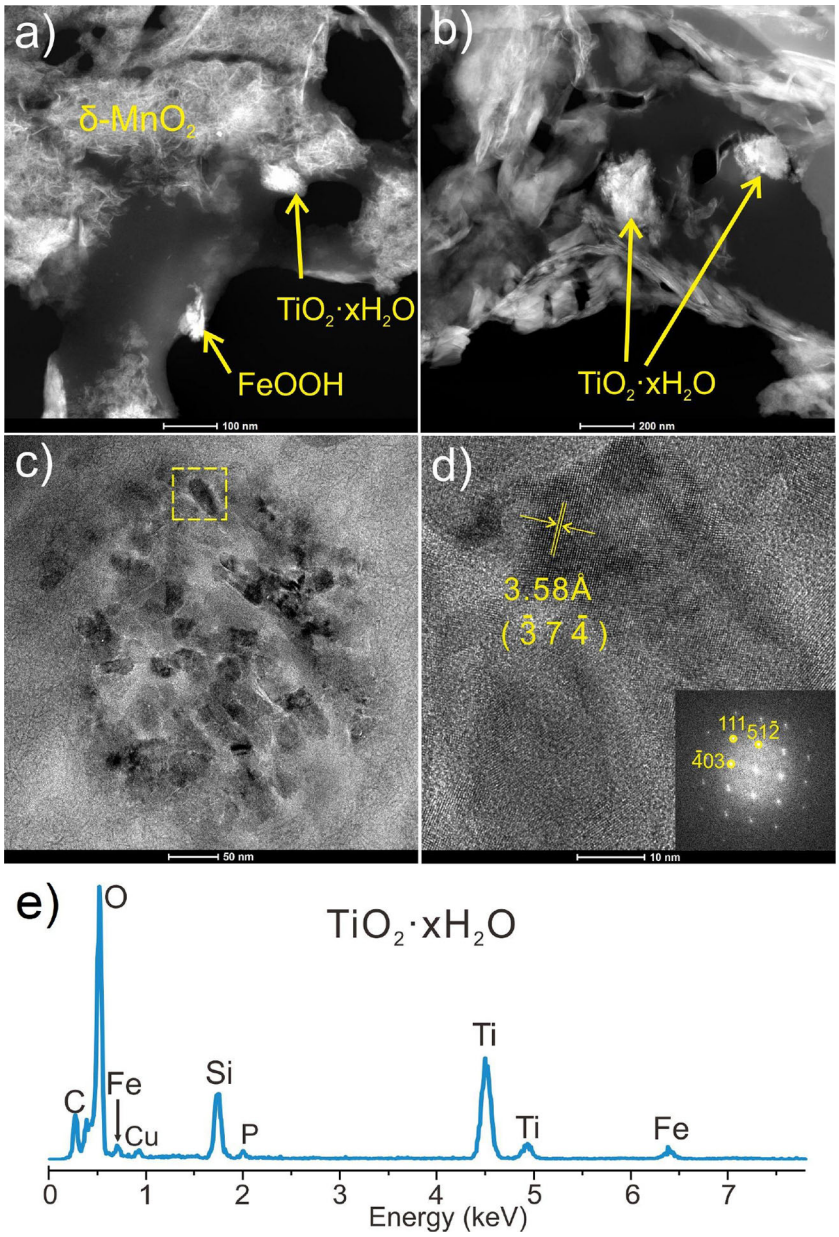

FIGURE 8
TEM photos, SAED and EDS patterns of nano-minerals in samples ST1 and ZJ86. **(A, B)** under the TEM dark field. **(C)** under bright field. **(D)**, high resolution image of the yellow dotted-line frame. **(E)** the energy spectra of the area inside the yellow dotted-line frame.

diagenesis to form todorokite, as reported in the Pacific and Atlantic Fe-Mn nodules and crusts (Marino et al., 2018). The Mn minerals in the SCS crusts and nodules are mainly disordered vernadite (δ-MnO_2) with minor birnessite and buserite. This result suggests that the SCS polymetallic crusts and nodules are mainly of hydrogenetic origin, with some Fe-Mn growth layers possibly affected by diagenesis (Guan et al., 2019).

Under the TEM bright field, we found direct evidence for the conversion of vernadite (δ-MnO_2) to birnessite and todorokite (Figure 10). Vernadite (δ-MnO_2) is an amorphous phyllomanganate that is randomly stacked in the c-axis. This series of δ-MnO_2 minerals is mainly divided into three species (Halbach et al., 2017): (1) 7 Å vernadite with [001] and [002] crystal plane spacing of ca. 7 and 3.5 Å, respectively; (2) 10 Å vernadite with [001] and [002] crystal plane spacing of ca. 10 and 5 Å, respectively; (3) Fe-vernadite (δ-MnO_2) without crystalline surface spacing, which is most common in the SCS polymetallic crusts and nodules (referred to as Fe-vernadite hereafter).

Birnessite are ordered, layered, well-crystallized δ-MnO_2 (Giovanoli, 1980). Since there are two species of 7 Å and 10 Å vernadite, the ordered birnessite is divided into 7 Å birnessite and 10 Å buserite. Birnessite is structurally more stable and occurs mostly in diagenetic (or mixed hydrogenetic-diagenetic) Fe-Mn crusts and nodules, which are often used as precursors in experiments on synthetic todorokite (Liu et al., 2005; Atkins et al., 2016). 10 Å buserite is more common in diagenetic Fe-Mn

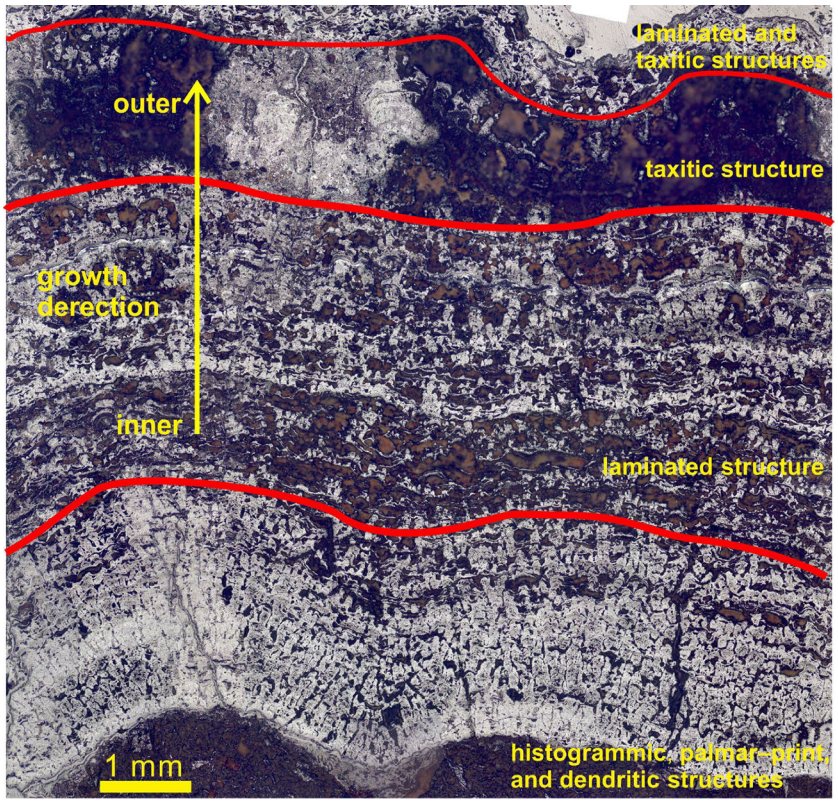

FIGURE 9
Microstructure growth of sample HYD66-1.

nodules, and can be used as a precursor (Bai et al., 2002) or intermediate transition phase (Bodeï et al., 2007) in experimental synthesis of the structurally less-stable todorokite.

The ideal todorokite has a 3-D tunnel structure, consisting of three M-O octahedra (arranged as tunnel) and three M-O octahedra (arranged as tunnel bottom) at common angles, with the tunnel and tunnel bottom oriented along the a-axis and c-axis, respectively (Yu, 1979; Cui et al., 2009; Qiao et al., 2016). Its [001] and [002] crystal plane spacing is ~9.7 Å and ~4.8 Å, respectively, and its diffraction pattern has a strong peak at ~2.4 Å and weak peaks at ~2.2 Å and ~1.7 Å.

As shown in Figure 10, Region 1 of the sample is a random stack of Mn oxides, whose diffraction patterns show two broad rings at ca. 2.4 and 1.4 Å, which indicates that δ-MnO_2 is weakly crystallized. In contrast, the minerals in Region 2 have a bamboo-leaf shape, and their diffraction patterns show four broad rings at ~4.9 Å, ~2.4 Å, ~2.1 Å, and ~1.4 Å, indicating that the nano-minerals in this region are relatively well crystallized. The HRTEM photos show clearer crystal plane stripes (Figures 10C, D), with crystal plane spacing of ca. 6.2 and 7.4 Å (birnessite) and 4.9 and 9.8 Å (todorokite).

To elucidate the transformation processes between these different Mn minerals, we combined our trace element data with published ones (Golden et al., 1987; Cui et al., 2005; Cui et al., 2006; Cui et al., 2010; Atkins et al., 2014; Lee and Xu, 2016b), and proposed a phase transformation model for Mn minerals in the SCS polymetallic crusts and nodules (Figure 11): the interlayer space of 7 Å birnessite contains single H_2O molecules and/or cations (e.g., Na^+, K^+, Mg^{2+}, Ca^{2+}, Ni^{2+}) (Manceau et al., 2014; Lee and Xu, 2016b; Halbach et al., 2017). Some cations (e.g., Ni^{2+}) can increase the layer spacing of birnessite after entering the layers of birnessite, which eventually leads to the conversion of 7 Å birnessite to todorokite (Golden et al., 1987; Atkins et al., 2016). This transformation process was also reported from Fe-Mn nodules in freshwater lakes (Lee and Xu, 2016b). Previous studies have shown that synthetic phyllomanganate mineral phases can be converted to todorokite by atmospheric reflux, hydrothermal treatment, or aging treatments (Cui et al., 2005; Cui et al., 2006; Cui et al., 2010; Atkins et al., 2016), and can be promoted by neutral-alkaline and reducing conditions and the presence of clay minerals. Since todorokite crystallization in the SCS polymetallic crusts and nodules is poor, we suggested that the SCS crusts and nodules were subjected to short period of suboxic conditions and diagenetic process.

The TEM-EDS results show that both birnessite and todorokite contain high Ni content, while vernadite (δ-MnO_2) contains only low trace element contents, which can be explained by their crystal structures. In the birnessite structure, some divalent cations (e.g., Co^{2+}, Ni^{2+}, Zn^{2+}, Fe^{2+}, Cu^{2+}) can replace Mn^{4+} to enter the Mn mineral interlayer (Halbach et al., 2017). In the todorokite, Mg^{2+}, Ca^{2+}, Co^{2+}, or Ba^{2+} are the main cations in the crystal lattice (Post, 1999; Manceau et al., 2014), while other cations are bound to the lamellar sites of Mn (incl. co-hexagonal, co-bilateral, co-trilateral, co-dual, and co-trigonal with Mn-O octahedra) (Cui et al., 2009; Qiao et al., 2016). In addition, vernadite has negative charge in seawater (Koschinsky and Hein, 2003), which facilitate its

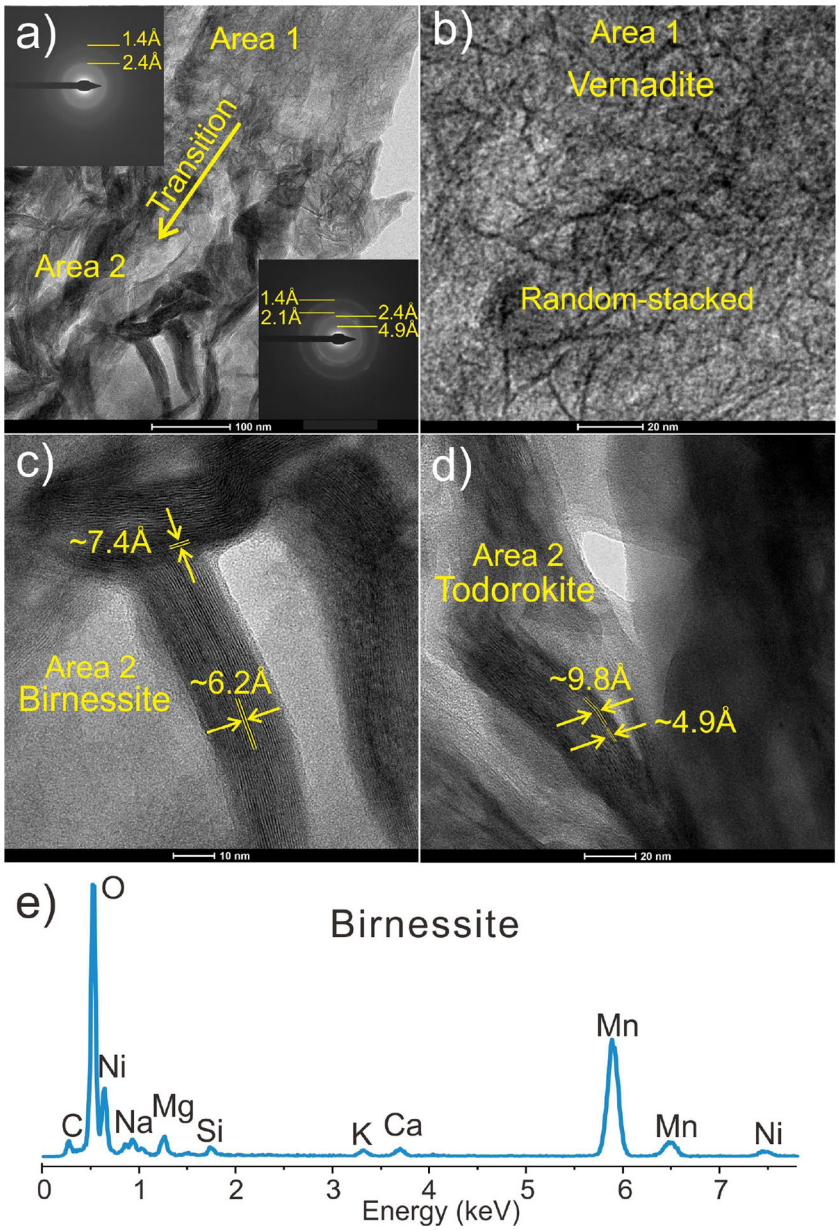

FIGURE 10
SAED patterns **(A)**, high resolution image **(B–D)**, and EDS pattern **(E)** of nano-minerals of sample ZJ86.

adsorption of free cations and cation complexes (e.g., VO^{2+}) from the seawater (Wehrli and Stumm, 1989).

6 Conclusions

(1) Growth structures of the SCS polymetallic crusts and nodules are mainly laminar, columnar, and mottled. The minerals include mainly vernadite (δ-MnO_2), quartz, feldspar, and amorphous FeOOH, as well as minor birnessite, todorokite, and clay minerals. Nano-minerals include mainly vernadite (δ-MnO_2), clay minerals, amorphous FeOOH, $H_2Ti_3O_7$, birnessite, and todorokite.

(2) Different mineral compositions and growth structures represent different growth environments. The growth environment of crusts and nodules from near the continental margin is relatively turbulent with significant terrigenous source influence. Meanwhile, the growth environment of crusts and nodules from near the central basin is more stable and less affected by terrigenous source.

(3) Titanium can form colloidal minerals in the seawater, and precipitate into the crusts and nodules with colloids such as FeOOH and Si-Al.

(4) Vernadite (δ-MnO_2) and birnessite can be transformed into the structurally more stable todorokite in suboxic environment. The SCS polymetallic crusts and nodules may have been in a short period of suboxic growth environment and diagenetic process.

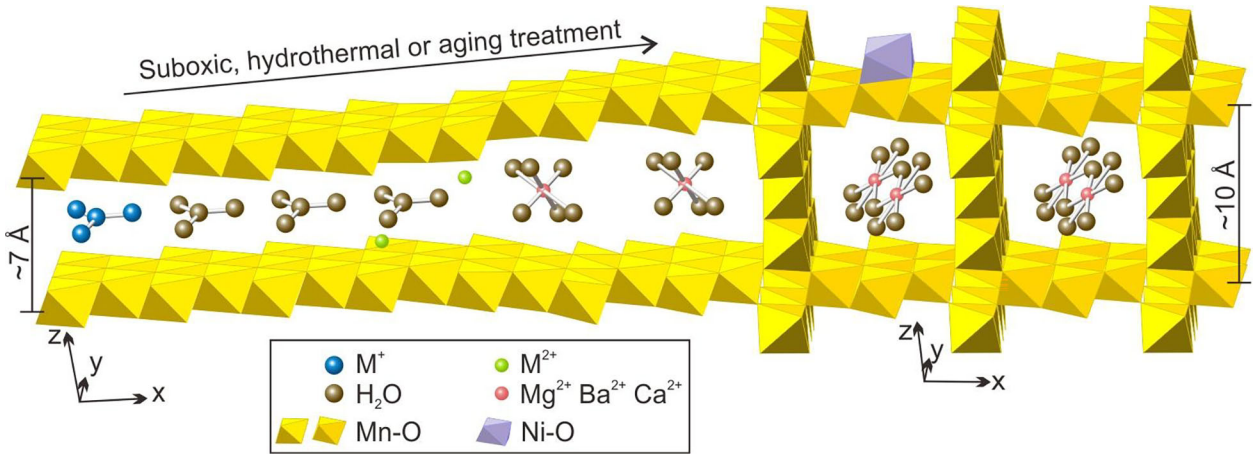

FIGURE 11
Schematic model of the Mn-oxides transformation in the SCS polymetallic crusts and nodules.

Data availability statement

The raw data supporting the conclusions of this article will be made available by the authors, without undue reservation.

Author contributions

YR, YG, and ZX conceived the experiments. YR analyzed the data and wrote this paper. YG participated in the writing of this paper. XS substantially revised the manuscript. LX, YD and WH analyzed the data and revised this paper. All authors contributed to the article and approved the submitted version.

Funding

This work is financially supported by National Natural Science Foundation of China (42003040, 92262304), Guangxi Natural Science Foundation Youth Science Foundation (2019GXNSFBA185030), and the Guangdong Provincial Key Laboratory of Marine Resources and Coastal Engineering Research Fund.

Acknowledgments

We thank the Guangzhou Marine Geological Survey for supplying the samples, and the Guangzhou Institute of Geochemistry, Chinese Academy of Sciences for helping with the mineralogical analysis. Many thanks to the editor and reviewers for their valuable advice.

Conflict of interest

The authors declare that the research was conducted in the absence of any commercial or financial relationships that could be construed as a potential conflict of interest.

Publisher's note

References

Akagi, T. (2013). Rare earth element (REE)-silicic acid complexes in seawater to explain the incorporation of REEs in opal and the "leftover" REEs in surface water: New interpretation of dissolved REE distribution profiles. *Geochim. Cosmochim. Acta* 113, 174–192. doi: 10.1016/j.gca.2013.03.014

Atkins, A. L., Shaw, S., and Peacock, C. L. (2014). Nucleation and growth of todorokite from birnessite: Implications for trace-metal cycling in marine sediments. *Geochim. Cosmochim. Acta* 144, 109–125. doi: 10.1016/j.gca.2014.08.014

Atkins, A. L., Shaw, S., and Peacock, C. L. (2016). Release of Ni from birnessite during transformation of birnessite to todorokite: Implications for Ni cycling in marine sediments. *Geochim. Cosmochim. Acta* 189, 158–183. doi: 10.1016/j.gca.2016.06.007

Bai, Z., Yin, C., Jiang, X., Liu, X., and Wang, S. (2002). Nanometer properties of oceanic polymetallic nodules and cobalt-rich crusts. *Chin. Sci. Bull.* 47, 15. doi: 10.1360/02tb9290

Bao, G., and Li, Q. (1993). Geochemistry of rare earth elements in ferromanganese nodules (crusts) of the south China Sea. *Oceanol. Limnol. Sin.* 24 (3), 304–313. doi: 10.3321/j.issn:0029-814X.1993.03.013

Bau, M., Schmidt, K., Koschinsky, A., Hein, J., Kuhn, T., and Usui, A. (2014). Discriminating between different genetic types of marine ferro-manganese crusts and nodules based on rare earth elements and yttrium. *Chem. Geol.* 381, 1–9. doi: 10.1016/j.chemgeo.2014.05.004

Bodeï, S., Manceau, A., Geoffroy, N., Baronnet, A., and Buatier, M. (2007). Formation of todorokite from vernadite in Ni-rich hemipelagic sediments. *Geochim. Cosmochim. Acta* 71, 5698–5716. doi: 10.1016/j.gca.2007.07.020

Bruland, K. W., Middag, R., and Lohan, M. C. (2014). "Controls of trace metals in seawater," in *Treatise on geochemistry (Second edition)*. Eds. H. D. Holland and K. K. Turekian (Oxford: Elsevier Ltd), 19–51.

Conrad, T., Hein, J. R., Paytan, A., and Clague, D. A. (2017). Formation of fe-Mn crusts within a continental margin environment. *Ore Geol. Rev.* 87, 25–40. doi: 10.1016/j.oregeorev.2016.09.010

Cui, H., Feng, X., He, J., Tan, W., and Liu, F. (2006). Effects of reaction conditions on the formation of todorokite at atmospheric pressure. *Clays Clay Minerals* 54, 605–615. doi: 10.1346/CCMN.2006.0540507

Cui, H., Feng, X., Liu, F., Tan, W., and He, J. (2005). Factors governing formation of todorokite at atmospheric pressure. *Sci. China—Series D: Earth Sci.* 48 (10), 1678–1689. doi: 10.1360/01yd0550

Cui, H., Feng, X., Liu, F., Tan, W., Qiu, G., and Chen, X. (2009). Progress in the study of todorokite. *Adv. Earth Sci.* 24 (10), 1085–1093. doi: 10.3321/j.issn:1001-8166.2009.10.003

Cui, H., Liu, F., Feng, X., Tan, W., and Wang, M. K. (2010). Aging promotes todorokite formation from layered manganese oxide at near-surface conditions. *J. Soils Sediments* 10, 1540–1547. doi: 10.1007/s11368-010-0261-z

Giovanoli, R. (1980). On natural and synthetic manganese nodules. *Geol. Geochem. Manganese* 1, 159–202.

Golden, D. C., Chen, C. C., and Dixon, J. B. (1987). Transformation of birnessite to buserite, todorokite, and manganite under mild hydrothermal treatment. *Clays Clay Minerals* 35, 271–280. doi: 10.1346/CCMN.1987.0350404

Grigoriev, A. G., Zhamoida, V. A., Gruzdov, K. A., and Krymsky, R. S. (2013). Age and growth rates of ferromanganese concretions from the gulf of Finland derived from 210Pb measurements. *Oceanology* 53 (3), 345–351. doi: 10.1134/S0001437013030041

Guan, Y., Ren, Z., Sun, X., Xiao, Z., and Huang, Y. (2019). Fine scale study of major and trace elements in the fe-Mn nodules from the south China Sea and their metallogenic constraints. *Mar. Geol.* 416, 105978. doi: 10.1016/j.margeo.2019.105978

Guan, Y., Sun, X., Jiang, X., Sa, R., Zhou, L., Huang, Y., et al. (2017a). The effect of fe-Mn minerals and seawater interface and enrichment mechanism of ore-forming elements of polymetallic crusts and nodules from the south China Sea. *Acta Oceanol. Sin.* 36 (6), 34–46. doi: 10.1007/s13131-017-1004-4

Guan, Y., Sun, X., Ren, Y., and Jiang, X. (2017b). Mineralogy, geochemistry and genesis of the polymetallic crusts and nodules from the south China Sea. *Ore Geol. Rev.* 89, 206–227. doi: 10.1016/j.oregeorev.2017.06.020

Guan, Y., Sun, X., Shi, G., Jiang, X., and Lu, H. (2017c). Rare earth elements composition and constraint on the genesis of the polymetallic crusts and nodules in the south China Sea. *Acta Geol. Sin. (English Edition)* 91 (5), 1751–1766. doi: 10.1111/1755-6724.13409

Halbach, P. E., Jahn, A., and Cherkashov, G. (2017). "Marine Co-rich ferromanganese crust deposits: Description and formation, occurrences and distribution, estimated world-wide resources," in *Deep-Sea minerals: Distribution characteristics and their resource potential*. Ed. R. Sharma (Switzerland: Springer Nature), 65–140.

Hein, J. R. (2005). Mercury- and silver-rich ferromanganese oxides, southern California borderland: Deposit model and environmental implications. *Economic Geol.* 100 (6), 1151–1168. doi: 10.2113/gsecongeo.100.6.1151

Hein, J. R., Koschinsky, A., Halbach, P., Manheim, F. T., and Bau, M. (1997). Iron and manganese oxide mineralization in the pacific. *Geol. Soc. London Special Publicat.* 119 (1), 123–138. doi: 10.1144/GSL.SP.1997.119.01.09

Hein, J. R., Mizell, K., Koschinsky, A., and Conrad, T. A. (2013). Deep-ocean mineral deposits as a source of critical metals for high- and green-technology applications: Comparison with land-based resources. *Ore Geol. Rev.* 51, 1–14. doi: 10.1016/j.oregeorev.2012.12.001

Izawa, H., Yasuda, F, ., Kikkawa, S., and Koizumi, M. (1985). Lithium ion titration of layered titanic acid, H2Ti3O7. *Chem. Lett.* 14, 1775–1778. doi: 10.1246/cl.1985.1775

Jiang, X., Lin, X., Yao, D., and Guo, W. (2011). Enrichment mechanisms of rare earth elements in marine hydrogenic ferromanganese crusts. *Sci. China Earth Sci.* 54 (2), 197–203. doi: 10.1007/s11430-010-4070-4

Jiang, X., Sun, X., and Guan, Y. (2019). Biogenic mineralization in the ferromanganese nodules and crusts from the south China Sea. *J. Asian Earth Sci.* 171, 46–59. doi: 10.1016/j.jseaes.2017.07.050

Kashiwabara, T., Takahashi, Y., Marcus, M. A., Uruga, T., Tanida, H., Terada, Y., et al. (2013). Tungsten species in natural ferromanganese oxides related to its different behavior from molybdenum in oxic ocean. *Geochim. Cosmochim. Acta* 106, 364–378. doi: 10.1016/j.gca.2012.12.026

Kataoka, K., Kijima, N., and Akimoto, J. (2013). Ion-exchange synthesis, crystal structure, and physical properties of hydrogen titanium oxide $H_2Ti_3O_7$. *Inorganic Chem.* 52, 13861–13864. doi: 10.1021/ic401144k

Konstantinova, N., Cherkashov, G., Hein, J. R., Mirão, J., Dias, L., Madureira, P., et al. (2017). Composition and characteristics of the ferromanganese crusts from the western Arctic ocean. *Ore Geol. Rev.* 87, 88–99. doi: 10.1016/j.oregeorev.2016.09.011

Konstantinova, N., Son, V. T., Thang, L. A., Trung, T. T., Giang, V. T., Dung, N. T. T., et al. (2022). Ferromanganese crusts of the Vietnam margin, central south China Sea: Composition and genesis. *Mar. Geol.* 453, 106911. doi: 10.1016/j.margeo.2022.106911

Koschinsky, A., and Halbach, P. (1995). Sequential leaching of marine ferromanganese precipitates: Genetic implications. *Geochim. Cosmochim. Acta* 59 (24), 5113–5132. doi: 10.1016/0016-7037(95)00358-4

Koschinsky, A., and Hein, J. R. (2003). Uptake of elements from seawater by ferromanganese crusts: Solid-phase associations and seawater speciation. *Mar. Geol.* 198 (3-4), 331–351. doi: 10.1016/S0025-3227(03)00122-1

Lee, S., Shen, Z., and Xu, H. (2016). Study on nanophase iron oxyhydroxides in freshwater ferromanganese nodules from green bay, lake Michigan, with implications for the adsorption of as and heavy metals. *Am. Mineral.* 101, 1986–1995. doi: 10.2138/am-2016-5729

Lee, S., and Xu, H. (2016a). Size-dependent phase map and phase transformation kinetics for nanometric iron(III) oxides ($\gamma \rightarrow \epsilon \rightarrow \alpha$ pathway). *J. Phys. Chem. C* 120 (24), 13316–13322. doi: 10.1021/acs.jpcc.6b05287

Lee, S., and Xu, H. (2016b). XRD and TEM studies on nanophase manganese oxides in freshwater ferromanganese nodules from green bay, lake Michigan. *Clays Clay Minerals* 64 (5), 523–536. doi: 10.1346/CCMN.2016.064032

Li, Z., and Zhang, F. (1990). Geochemical of elements in ferromanganese particles at depths of south Sea. *Mar. Sci. Bull.* 9 (6), 41–50.

Lin, Z., Ji, F., Zhang, F., Lin, X., and Shi, Z. (2003). Characteristics and origin of ferromanganese nodules from the northeastern continental slope of the south China Sea. *Mar. Geol. Quater. Geol.* 23 (1), 7–12.

Liu, Z.h., Kang, L., Ooi, K., Makita, Y., and Feng, Q. (2005). Studies on the formation of todorokite-type manganese oxide with different crystalline birnessites by Mg2+-templating reaction. *J. Colloid Interface Sci.* 285, 239–246. doi: 10.1016/j.jcis.2004.11.021

Manceau, A., Lanson, M., and Takahashi, Y. (2014). Mineralogy and crystal chemistry of Mn, fe, Co, Ni, and Cu in a deep-sea pacific polymetallic nodule. *Am. Mineral.* 99 (10), 2068–2083. doi: 10.2138/am-2014-4742

Marcus, M. A., Edwards, K. J., Gueguen, B., Fakra, S. C., Horn, G., Jelinski, N. A., et al. (2015). Iron mineral structure, reactivity, and isotopic composition in a south pacific gyre ferromanganese nodule over 4 ma. *Geochim. Cosmochim. Acta* 171, 61–79. doi: 10.1016/j.gca.2015.08.021

Marino, E., González, F. J., Lunar, R., Reyes, J., Medialdea, T., Castillo-Carrión, M., et al. (2018). High-resolution analysis of critical minerals and elements in fe-Mn crusts from the canary island seamount province (Atlantic ocean). *Minerals* 8 (7), 285. doi: 10.3390/min8070285

Pattan, J. N., and Parthiban, G. (2007). Do manganese nodules grow or dissolve after burial? results from the central Indian ocean basin. *J. Asian Earth Sci.* 30 (5-6), 696–705. doi: 10.1016/j.jseaes.2007.03.003

Pelleter, E., Fouquet, Y., Etoubleau, J., Cheron, S., Labanieh, S., Josso, P., et al. (2017). Ni-Cu-Co-rich hydrothermal manganese mineralization in the Wallis and Futuna back-arc environment (SW pacific). *Ore Geol. Rev.* 87, 126–146. doi: 10.1016/j.oregeorev.2016.09.014

Post, J. E. (1999). Manganese oxide minerals: Crystal structures and economic and environmental significance. *Proc. Natl. Acad. Sci.* 96 (7), 3447–3454. doi: 10.1073/pnas.96.7.3447

Qiao, Z., Tu, X., and Zhou, H. (2016). Microscopic characteristics of manganates in deep sea ferromanganese nodules. *Chin. J. Nat.* 38 (4), 1–8. doi: 10.3969/j.issn.0253-9608.2016.04.006

Rajani, R. P., Banakar, V. K., Parthiban, G., Mudholkar, A. V., and Chodankar, A. R. (2005). Compositional variation and genesis of ferromanganese crusts of the afanasiy–nikitin seamount, equatorial Indian ocean. *J. Earth System Sci.* 114 (1), 51–61. doi: 10.1007/BF02702008

Shiraishi, F., Mitsunobu, S., Suzuki, K., Hoshino, T., Morono, Y., and Inagaki, F. (2016). Dense microbial community on a ferromanganese nodule from the ultra-oligotrophic south pacific gyre: Implications for biogeochemical cycles. *Earth Planet. Sci. Lett.* 447, 10–20. doi: 10.1016/j.epsl.2016.04.021

Takahashi, Y., Manceau, A., Geoffroy, N., Marcus, M. A., and Usui, A. (2007). Chemical and structural control of the partitioning of Co, ce, and Pb in marine ferromanganese oxides. *Geochim. Cosmochim. Acta* 71 (4), 984–1008. doi: 10.1016/j.gca.2006.11.016

Tréguer, P. J., and de la Rocha, C. L. (2013). The world ocean silica cycle. *Annu. Rev. Mar. Sci.* 5 (5), 477–501. doi: 10.1146/annurev-marine-121211-172346

Usui, A., Mellin, T. A., Nohara, M., and Yuasa, M. (1989). Structural stability of marine 10Å manganates from the ogasawara (Bonin) arc: Implication for low-temperature hydrothermal activity. *Mar. Geol.* 86, 41–56. doi: 10.1016/0025-3227(89)90017-0

Usui, A., Nishi, K., Sato, H., Nakasato, Y., Thornton, B., Kashiwabara, T., et al. (2017). Continuous growth of hydrogenetic ferromanganese crusts since 17 myr ago on takuyo-daigo seamount, NW pacific, at water depths of 800-5500 m. *Ore Geol. Rev.* 87, 71–87. doi: 10.1016/j.oregeorev.2016.09.032

Wang, P., and Li, Q. (2009). "The south China Sea," in *The south China Sea*. Eds. P. Wang and Q. Li (Berlin: Springer), 28–56.

Wang, Y., and Zhang, Z. (2011). Internal microstructure characteristics and geological significance of polymetallic nodules from the northern continental margin of the south China Sea. *J. North China Univ. Sci. Technol. (Natural Sci. Edition)* 33 (4), 5–8. doi: 10.3969/j.issn.1674-0262.2011.04.002

Wehrli, B., and Stumm, W. (1989). Vanadyl in natural waters: Adsorption and hydrolysis promote oxygenation. *Geochim. Cosmochim. Acta* 53, 69–77. doi: 10.1016/0016-7037(89)90273-1

Xu, D. (2013). *Ocean mineral geology* (Beijing: Ocean Press).

Yang, S., Qiu, Y., and Zhu, B. (2015). *Atlas of geology and geophysics of the south China Sea* (Tianjin: China Navigation Publications).

Yli-Hemminki, P., Sara-Aho, T., Jørgensen, K. S., and Lehtoranta, J. (2016). Iron–manganese concretions contribute to benthic release of phosphorus and arsenic in anoxic conditions in the Baltic Sea. *J. Soils Sediments* 16 (8), 2138–2152. doi: 10.1007/s11368-016-1426-1

Yu, X. (1979). Mineral structure of deep-sea manganese nodules. *Mar. Sci.* 3 (2), 44–50.

Zhang, Z., Du, Y., Wu, C., Fang, N., Yang, S., Liu, J., et al. (2013). Growth of a polymetallic nodule from northwestern continental margin of the south China Sea and its response to changes in paleoceanographical environment of the late Cenozoic. *Sci. China: Earth Sci.* 56, 453–463. doi: 10.1007/s11430-012-4535-8

Zhang, Z., Fang, N., Du, Y., Gao, L., Yang, S., Liu, J., et al. (2009). Geochemical characteristics and their causative mechanism of polymetallic nodules from the northwest continental margin of the south China Sea. *Earth Sci.* 34 (6), 955–962. doi: 10.3321/j.issn:1000-2383.2009.06.010

Zhang, X., and Weng, H. (2005). Deposit record of iron and manganese in northeast continental slope of the south China Sea and its indication to environmental changes. *Haiyang Xuebao* 27 (1), 93–100. doi: 10.3321/j.issn:0253-4193.2005.01.013

Zhong, Y., Chen, Z., González, F. J., Hein, J. R., Zheng, X., Li, G., et al. (2017). Composition and genesis of ferromanganese deposits from the northern south China Sea. *J. Asian Earth Sci.* 138, 110–128. doi: 10.1016/j.jseaes.2017.02.015

Zhong, Y., Liu, Q., Chen, Z., Gonzáleze, F. J., Hein, J. R., Zhang, J., et al. (2019). Tectonic and paleoceanographic conditions during the formation of ferromanganese nodules from the northern south China Sea based on the high-resolution geochemistry, mineralogy and isotopes. *Mar. Geol.* 410, 146–163. doi: 10.1016/j.margeo.2018.12.006

Zhou, H. (2016). Metallogenetic mystery of deep sea ferromanganese nodules. *Chin. J. Nat.* 37 (6), 397–404. doi: 10.3969/j.issn:0253-9608.2015.06.001

Zhou, J., Cai, P. J., Yang, C. P., Li, X. J., Gao, H. F., Cai, G. Q., et al. (2021). Geochemical characteristics and genesis of polymetallic crusts in the seamount chain of the Eastern subsean basin, south China Sea. *Earth Sci.* 47 (7), 2586–2601. doi: 10.3799/dqkx.2021.093